

The electroweak precision constraints of the 2HDM+S

Cheng Li^a , Juxiang Li^a , Shufang Su^b and Wei Su^{a,c}

^a*School of Science, Shenzhen Campus of Sun Yat-sen University, No. 66, Gongchang Road, Guangming District, Shenzhen, Guangdong 518107, China*

^b*Department of Physics, University of Arizona, Tucson, AZ 85721, U.S.A.*

^c*Institute of Theoretical Physics, Chinese Academy of Sciences, Beijing 100190, P. R. China*

E-mail: lich389@mail.sysu.edu.cn, lijx376@mail2.sysu.edu.cn,
suwei26@mail.sysu.edu.cn, shufang@email.arizona.edu

ABSTRACT: The 2HDM+S is the singlet extension of the Two-Higgs-Doublets Model (2HDM). The singlet field and its mixing with the 2HDM Higgs sector lead to new contributions to the electroweak precision observables, in particular, the oblique parameters. In this paper, we identify five benchmark cases, where at most one mixing angle is nonzero and analyze the 95% C.L. allowed parameter space by the oblique parameters. In the alignment limit of the 2HDM, we find that other than the usual mass relations of $m_H \sim m_{H^\pm}$ or $m_A \sim m_{H^\pm}$, electroweak precision measurements also impose an upper limit on the neutral Higgs masses. In the cases with nonzero singlet mixing with the 2HDM Higgses H or A , we find approximate mass relations of $c_{\alpha_{HS}}^2 m_H + s_{\alpha_{HS}}^2 m_{h_S} = m_{H^\pm}$ or $c_{\alpha_{AS}}^2 m_A + s_{\alpha_{AS}}^2 m_{A_S} = m_{H^\pm}$. Those relations are universal to the 2HDM+S models, with or without further symmetry assumption. We also study the non-alignment limit of the 2HDM+S, which typically has tighter constraints on the masses and mixing angles. At the end, we examine the complementarity between the electroweak precision analyses and the Higgs coupling precision measurements.

KEYWORDS: Electroweak precision observables

Contents

1	Introduction	1
2	Theoretical framework	3
3	Oblique parameters	6
4	Five Benchmark Cases	9
4.1	Case-0	9
4.2	Case-I: $c_{\beta-\alpha} \neq 0$	10
4.3	Case-II: $\alpha_{hS} \neq 0$	13
4.4	Case-III: $\alpha_{HS} \neq 0$	14
4.5	Case-IV: $\alpha_{AS} \neq 0$	16
5	The STU constraints beyond the alignment limit	17
6	Interplay of electroweak and Higgs precision measurements	20
7	Conclusions	21
A	Appendix	23

1 Introduction

Electroweak precision observables have provided a precise test of the Standard Model (SM) at the loop level [1, 2], which are consistent with the observations of a 125 GeV SM-like Higgs [3, 4]. However, SM could not provide satisfactory solutions to dark matter, neutrino mass, baryogenesis, etc.[5–8]. Furthermore, the naturalness problem in the SM also points to new physics beyond the SM [9].

One of the simplest extensions of the SM Higgs sector is the Two-Higgs doublet model (2HDM) [10], which has been studied extensively in the literature. The 2HDM can be further extended by an additional singlet field, which is the N2HDM with a real singlet [11] and the 2HDM+S with a complex singlet [12]. The 2HDM+S matches to the Next-to Minimal Supersymmetric Standard Model (NMSSM) [13] at low energy scale, and can provide a dark matter candidate [14], as well as accommodate the possible 95 GeV excess at the LEP and the LHC [15]. The phenomenological properties of 2HDM+S have only been explored in some specific scenarios, while the more general cases of 2HDM+S have not yet been studied in detail. In this work, we explore the implications of the electroweak precision measurements

on the 2HDM+S parameter space. In particular, we focus on the oblique parameters S , T and U , which are sensitive to the new physics contributions to the W and Z self-energies [16].

The scalar sector of 2HDM + S includes two $SU(2)_L$ doublets and a complex singlet. The singlet field does not couple to the SM gauge bosons and fermions. After the neutral components get vacuum expectation values (vev), assuming no CP-violation, the mass spectrum of the Higgs sectors includes 3 CP-even scalars, two CP-odd scalars, and a pair of charged Higgses. In particular, the CP-even and CP-odd singlet components mix with the corresponding ones in the $SU(2)_L$ doublets, which leads to the couplings of the singlet-like scalars to the SM gauge bosons, as well as modifies the couplings of the doublet-like scalars to the SM sector. The most general 2HDM+S Higgs potential has 27 free parameters, and eleven of those can be chosen to be the masses of the Higgs bosons, as well as the mixing angles between Higgses. The remaining parameters in the Higgs potential are the Higgs self-couplings, which do not directly contribute to the oblique parameters. Therefore, in our study, we only focus on those eleven mass and mixing parameters. We parametrize such mixing parameters by α_{hS} , the mixing of the CP-even singlet with the 125 GeV SM-like Higgs h , α_{HS} , the mixing of the CP-even singlet with the 2HDM CP-even Higgs H , and α_{AS} , the mixing of the CP-odd singlet with the 2HDM CP-odd Higgs A . Including the usual 2HDM mixing angle of the CP-even Higgses α , we introduce five basic benchmark scenarios, Case-0 for the 2HDM alignment limit and Case-I – IV in which only one mixing angle is set to be nonzero. We analyze the contributions to the oblique parameters in each case and study the 95% C.L. allowed region in the relevant parameter spaces under the oblique parameters. After the discussion of these five benchmark scenarios, we also discuss the cases with a non-zero singlet mixing angle away from the alignment limit.

The implications of electroweak precision measurements in the 2HDM have been studied in the literature [17, 18]. Our study offers a comprehensive electroweak precision analysis of 2HDM+S and identifies the impact of each singlet mixing angle. Since only the couplings between the Higgses and the SM gauge bosons enter the oblique parameters, our results are universal to the 2HDM+S models, with or without further symmetry assumption of the Higgs potential. In addition, we explore the complementarity of the electroweak precision analyses with the Higgs precision measurements.

The remainder of the paper is organized as follows. In [Section 2](#), we introduce the theoretical framework of 2HDM + S, as well as five benchmark cases. In [Section 3](#), we introduce the electroweak oblique parameters and the contributions from the Higgs sector in the 2HDM+S. In [Section 4](#), we present 95% C.L. STU allowed regions in the 2HDM+S parameter spaces of the five benchmark cases. In [Section 5](#), we study the cases beyond the alignment limit. In [Section 6](#), we show the complementarity of electroweak precision analyses with Higgs precision measurements. We conclude in [Section 7](#).

2 Theoretical framework

The 2HDM+S is the singlet extension of the 2HDM, which has the following scalar contents:

$$\Phi_1 = \begin{pmatrix} \chi_1^+ \\ \frac{\rho_1 + i\eta_1}{\sqrt{2}} \end{pmatrix}, \quad \Phi_2 = \begin{pmatrix} \chi_2^+ \\ \frac{\rho_2 + i\eta_2}{\sqrt{2}} \end{pmatrix}, \quad S = \frac{\rho_S + i\eta_S}{\sqrt{2}}, \quad (2.1)$$

where Φ_1, Φ_2 are the $SU(2)_L$ doublets with hypercharge $Y = 1/2$, and S is the gauge singlet. The general Higgs potential of 2HDM+S has been introduced in [12], while the simplified version of the 2HDM+S potential can be found in [15] when certain symmetries are imposed. After electroweak symmetry breaking, the neutral components of Φ_1, Φ_2 and S develop non-zero vacuum expectation values, v_1, v_2 and v_S , with $\sqrt{v_1^2 + v_2^2} = v \approx 246$ GeV. We also introduce $\tan \beta = \frac{v_2}{v_1}$ with $\beta \in (0, \pi/2)$. Assuming no CP-violation, the mass spectrum of the 2HDM+S includes three neutral CP-even scalars, two neutral CP-odd scalars, and one pair of charged Higgs bosons.

The neutral CP-even states, $\rho_{1,2,S}$ mix together to form three mass eigenstates: the Non-SM-like H , the SM-like Higgs h and the singlet-like h_S , with the 3×3 rotation matrix R

$$\begin{pmatrix} H \\ h \\ h_S \end{pmatrix} = R \begin{pmatrix} \rho_1 \\ \rho_2 \\ \rho_S \end{pmatrix}, \quad RM_S^2 R^T = \text{diag}\{m_H^2, m_h^2, m_{h_S}^2\}. \quad (2.2)$$

the R matrix is parametrized by three mixing angles α, α_{HS} , and α_{hS} , which characterize the mixing angle between the two neutral components of the Higgs doublets $\rho_{1,2}$, and the mixing angles between the singlet ρ_S with the 2HDM CP-even Higgses:

$$\begin{aligned} R &= \begin{pmatrix} 1 & 0 & 0 \\ 0 & c_{\alpha_{hS}} & s_{\alpha_{hS}} \\ 0 & -s_{\alpha_{hS}} & c_{\alpha_{hS}} \end{pmatrix} \begin{pmatrix} c_{\alpha_{HS}} & 0 & s_{\alpha_{HS}} \\ 0 & 1 & 0 \\ -s_{\alpha_{HS}} & 0 & c_{\alpha_{HS}} \end{pmatrix} \begin{pmatrix} c_\alpha & s_\alpha & 0 \\ -s_\alpha & c_\alpha & 0 \\ 0 & 0 & 1 \end{pmatrix} \\ &= \begin{pmatrix} c_\alpha c_{\alpha_{HS}} & s_\alpha c_{\alpha_{HS}} & s_{\alpha_{HS}} \\ -s_\alpha c_{\alpha_{hS}} - c_\alpha s_{\alpha_{HS}} s_{\alpha_{hS}} & c_\alpha c_{\alpha_{hS}} - s_\alpha s_{\alpha_{HS}} s_{\alpha_{hS}} & c_{\alpha_{HS}} s_{\alpha_{hS}} \\ s_\alpha s_{\alpha_{hS}} - c_\alpha s_{\alpha_{HS}} c_{\alpha_{hS}} & -s_\alpha s_{\alpha_{HS}} c_{\alpha_{hS}} - c_\alpha s_{\alpha_{hS}} & c_{\alpha_{HS}} c_{\alpha_{hS}} \end{pmatrix}, \end{aligned} \quad (2.3)$$

where we use the shorthand notation $s_x = \sin x$ and $c_x = \cos x$. For the CP-odd states, we have

$$\begin{pmatrix} G^0 \\ A \\ A_S \end{pmatrix} = \begin{pmatrix} 1 & 0 & 0 \\ 0 & R^A \\ 0 & & \end{pmatrix} \begin{pmatrix} c_\beta & s_\beta & 0 \\ -s_\beta & c_\beta & 0 \\ 0 & 0 & 1 \end{pmatrix} \begin{pmatrix} \eta_1 \\ \eta_2 \\ \eta_S \end{pmatrix}, \quad R^A = \begin{pmatrix} c_{\alpha_{AS}} & s_{\alpha_{AS}} \\ -s_{\alpha_{AS}} & c_{\alpha_{AS}} \end{pmatrix}, \quad (2.4)$$

where G^0 is the neutral Goldstone boson, and the angle α_{AS} is the mixing between the 2HDM pseudoscalar and the singlet pseudoscalar η_S . In addition, the charged sector of the 2HDM+S is the same as the 2HDM, containing one pair of charged Higgses H^\pm and the Goldstone bosons G^\pm . Each of the mixing angles $\alpha, \alpha_{HS}, \alpha_{hS}, \alpha_{AS}$ varies in the range of

$$-\frac{\pi}{2} < \alpha_i < \frac{\pi}{2}. \quad (2.5)$$

When $\alpha_i = \pm \frac{\pi}{4}$, the mixing between the two Higgs bosons reaches maximum, and the properties of the two corresponding scalars flip when $\frac{\pi}{4} < |\alpha_i| < \frac{\pi}{2}$. Note that the effects of different signs of the mixing angles enter only when all four mixing angles are nonzero. When at least one mixing angle is nonzero, the properties of the Higgs bosons are independent of the sign of the mixing angles.

After the diagonalization of the Higgs mass matrices, there are 11 free parameters for the mass eigenstates: six Higgs boson masses, $\tan \beta$ and four mixing angles. Since only the couplings between the Higgses and the SM gauge bosons enter the oblique parameters, we focus on the following nine free parameters for our study of the oblique parameters:

$$\underbrace{m_h = 125 \text{ GeV}, m_H, m_A, m_{H^\pm}, \cos(\beta - \alpha)}_{\text{2HDM parameters}}, \underbrace{m_{h_S}, m_{A_S}, \alpha_{HS}, \alpha_{hS}, \alpha_{AS}}_{\text{singlet parameters}}. \quad (2.6)$$

Using the mixing matrices, one can obtain the couplings of physical Higgses to the gauge bosons, which are denoted by the following effective couplings

$$g_{h_i V V}^{\mu\nu} = c_{h_i V V} i \frac{2m_V^2}{v} g^{\mu\nu}, \quad (2.7)$$

where h_i represents all possible neutral CP-even states, including h , H , and h_S , and $V = W, Z$. The normalized couplings $c_{h_i V V}$ are shown in Table 1.

In addition, the gauge boson can couple to two different Higgs bosons: the Z boson couples to two Higgs bosons with different CP properties and the W bosons couple to neutral and charged Higgs bosons. These interactions can be parametrized as

$$g_{\phi_i \varphi_j V}^\mu = c_{\phi_i \varphi_j V} i \frac{m_V}{v} (p_{\phi_i}^\mu - p_{\varphi_j}^\mu), \quad (2.8)$$

$$g_{H^- H^+ \gamma}^\mu = c_{H^- H^+ \gamma} i e (p_{H^-}^\mu - p_{H^+}^\mu), \quad (2.9)$$

$$g_{H^- H^+ Z}^\mu = c_{H^- H^+ Z} i e \frac{c_W^2 - s_W^2}{s_W c_W} (p_{H^-}^\mu - p_{H^+}^\mu), \quad (2.10)$$

where ϕ_i, φ_j correspond to different types of Higgs bosons and φ includes neutral states ϕ and charged Higgs H^\pm ¹. Furthermore, the Higgs bosons can couple to gauge bosons via the quartic interactions, which are

$$g_{\phi_i \varphi_j V V}^{\mu\nu} = c_{\phi_i \varphi_j V V} \frac{i 2m_V^2}{v^2} g^{\mu\nu}. \quad (2.11)$$

Given the complexity of the 2HDM+S scalar sectors and the appearance of multiple mixing angles, we consider five benchmark cases to disentangle the impact of each mixing angle. For the Case-0, we have all mixing angles set to be 0, which is the 2HDM alignment limit case. For other cases, only one mixing angle is nonzero while the others are fixed to 0, as shown in Table 1.

¹The notation of ϕ_i represent all possible neutral Higgs bosons, including h , H , h_S , A , and A_S . The notation of φ_j represent all possible Higgs bosons, including h , H , h_S , A , A_S and H^\pm . The general expression of $\phi_i \varphi_j V$ couplings include the couplings of $a_i h_j Z$, $a_i H^\pm W^\mp$ and $h_i H^\pm W^\mp$, where a_i represents A and A_S , and h_j represents h , H and h_S .

Benchmark Case	Fixed mixing angles	Variable mixing angles
Case-0 (2HDM alignment limit)	$c_{\beta-\alpha} = \alpha_{HS} = \alpha_{hS} = \alpha_{AS} = 0$	—
Case-I (2HDM limit)	$\alpha_{HS} = \alpha_{hS} = \alpha_{AS} = 0$	$c_{\beta-\alpha}$
Case-II (SSM limit)	$c_{\beta-\alpha} = \alpha_{HS} = \alpha_{AS} = 0$	α_{hS}
Case-III	$c_{\beta-\alpha} = \alpha_{hS} = \alpha_{AS} = 0$	α_{HS}
Case-IV	$c_{\beta-\alpha} = \alpha_{hS} = \alpha_{HS} = 0$	α_{AS}

Table 1. Five benchmark cases for the mixing angles configuration.

- Case-0 with $c_{\beta-\alpha} = \alpha_{HS} = \alpha_{hS} = \alpha_{AS} = 0$ is the 2HDM alignment limit, where the singlet components are decoupled and 125 GeV Higgs h is the same as the SM Higgs. In this case, all the couplings of the singlet Higgs bosons h_S , A_S to SM particles are zero, and the beyond the SM (BSM) Higgs coupling HVV is zero. However, the BSM Higgs bosons can still couple to gauge bosons via AHZ , $HH^\pm W^\mp$, $AH^\pm W^\mp$, $HHVV$, $AAVV$ and H^+H^-VV couplings.
- Case-I with $\alpha_{HS} = \alpha_{hS} = \alpha_{AS} = 0$ is the 2HDM limit, when the singlet components are completely decoupled. The mixing between H and h is parameterized by α , as in the usual 2HDM.
- Case-II with $\alpha_{hS} \neq 0$ represents the case when the 125 GeV h mixes with the singlet Higgs h_S , thus the SM-like Higgs properties are similar to those of the singlet extended SM (SSM). But the BSM doublet components H/A are the same as the alignment limit of the 2HDM.
- Case-III with $\alpha_{HS} \neq 0$ represents the case when the non-SM H mixes with the singlet Higgs h_S , while the 125 GeV Higgs h is completely SM-like.
- Case-IV with $\alpha_{AS} \neq 0$ represents the case when A mixes with the singlet pseudoscalar A_S , where the CP-even sector is the same as the alignment limit of the 2HDM, plus a decoupled singlet scalar S .

In Table. 2, we list the couplings between the Higgses and the SM gauge bosons, which are relevant for the calculation of the oblique parameters. The general expressions are given in the second column, as well as the couplings in the individual Case-0 – Case-IV. Since the STU parameters only depend on couplings between the Higgses and gauge bosons, the fermionic couplings of the Higgs bosons are irrelevant in this study. Therefore, the contributions to the STU parameters are independent of the specific structure of the Yukawa couplings. In particular, when the singlet CP-odd Higgs is decoupled by $\alpha_{AS} = 0$, the 2HDM+S is similar to the N2HDM (the real singlet extension of 2HDM [11]). Note that, the $A_S h Z$ and $A_S h_S Z$ couplings are always zero for these benchmark cases, since multiple non-zero mixing angles are needed to couple the CP-odd singlet Higgs A_S to the CP-even Higgs h and h_S . In addition,

	Couplings	Case-0	Case-I	Case-II	Case-III	Case-IV
$c_{h_i V V} = R_{i1} c_\beta + R_{i2} s_\beta$						
c_{HVV}	$c_{\beta-\alpha} c_{\alpha_{HS}}$	0	$c_{\beta-\alpha}$	0	0	0
c_{hVV}	$s_{\beta-\alpha} c_{\alpha_{hS}} - c_{\beta-\alpha} s_{\alpha_{HS}} s_{\alpha_{hS}}$	1	$s_{\beta-\alpha}$	$c_{\alpha_{hS}}$	1	1
$c_{h_S VV}$	$-s_{\beta-\alpha} s_{\alpha_{hS}} - c_{\beta-\alpha} s_{\alpha_{HS}} c_{\alpha_{hS}}$	0	0	$-s_{\alpha_{hS}}$	0	0
$c_{a_i h_j Z} = R_{i1}^A R_{j1} + R_{i2}^A R_{j2}$						
c_{AHZ}	$-c_{\alpha_{AS}} c_{\alpha_{HS}} s_{\beta-\alpha}$	-1	$-s_{\beta-\alpha}$	-1	$-c_{\alpha_{HS}}$	$-c_{\alpha_{AS}}$
c_{AhZ}	$c_{\alpha_{AS}} \left(c_{\beta-\alpha} c_{\alpha_{hS}} + s_{\beta-\alpha} s_{\alpha_{HS}} s_{\alpha_{hS}} \right)$	0	$c_{\beta-\alpha}$	0	0	0
$c_{Ah_S Z}$	$-c_{\alpha_{AS}} \left(c_{\beta-\alpha} s_{\alpha_{hS}} - s_{\beta-\alpha} s_{\alpha_{HS}} c_{\alpha_{hS}} \right)$	0	0	0	$s_{\alpha_{HS}}$	0
$c_{A_S HZ}$	$s_{\alpha_{AS}} c_{\alpha_{HS}} s_{\beta-\alpha}$	0	0	0	0	$s_{\alpha_{AS}}$
$c_{A_S hZ}$	$-s_{\alpha_{AS}} \left(c_{\beta-\alpha} c_{\alpha_{hS}} + s_{\beta-\alpha} s_{\alpha_{HS}} s_{\alpha_{hS}} \right)$	0	0	0	0	0
$c_{A_S h_S Z}$	$s_{\alpha_{AS}} \left(c_{\beta-\alpha} s_{\alpha_{hS}} - s_{\beta-\alpha} s_{\alpha_{HS}} c_{\alpha_{hS}} \right)$	0	0	0	0	0
$c_{\phi_i H^\pm W^\mp} = R_{i2}^\phi c_\beta - R_{i1}^\phi s_\beta$						
$c_{HH^\pm W^\mp}$	$-i c_{\alpha_{HS}} s_{\beta-\alpha}$	-i	$-i s_{\beta-\alpha}$	-i	$-i c_{\alpha_{HS}}$	-i
$c_{hH^\pm W^\mp}$	$i \left(c_{\beta-\alpha} c_{\alpha_{hS}} + s_{\beta-\alpha} s_{\alpha_{HS}} s_{\alpha_{hS}} \right)$	0	$i c_{\beta-\alpha}$	0	0	0
$c_{h_S H^\pm W^\mp}$	$-i \left(c_{\beta-\alpha} s_{\alpha_{hS}} - s_{\beta-\alpha} s_{\alpha_{HS}} c_{\alpha_{hS}} \right)$	0	0	0	$-i s_{\alpha_{HS}}$	0
$c_{AH^\pm W^\mp}$	$c_{\alpha_{AS}}$	1	1	1	1	$c_{\alpha_{AS}}$
$c_{A_S H^\pm W^\mp}$	$-s_{\alpha_{AS}}$	0	0	0	0	$-s_{\alpha_{AS}}$
$c_{\phi_i \phi_j VV} = R_{i1}^\phi R_{j1}^\phi + R_{i2}^\phi R_{j2}^\phi$						
c_{HHVV}	$c_{\alpha_{HS}}^2$	1	1	1	$c_{\alpha_{HS}}^2$	1
c_{hhVV}	$c_{\alpha_{hS}}^2 + s_{\alpha_{HS}}^2 s_{\alpha_{hS}}^2$	1	1	$c_{\alpha_{hS}}^2$	1	1
$c_{h_S h_S VV}$	$c_{\alpha_{hS}}^2 s_{\alpha_{HS}}^2 + s_{\alpha_{hS}}^2$	0	0	$s_{\alpha_{hS}}^2$	$s_{\alpha_{HS}}^2$	0
c_{HhVV}	$-\frac{1}{2} s_{2\alpha_{HS}} s_{\alpha_{hS}}$	0	0	0	0	0
$c_{Hh_S VV}$	$-\frac{1}{2} s_{2\alpha_{HS}} c_{\alpha_{hS}}$	0	0	0	$-\frac{1}{2} s_{2\alpha_{HS}}$	0
$c_{hh_S VV}$	$-\frac{1}{2} c_{\alpha_{HS}}^2 s_{2\alpha_{hS}}$	0	0	$-\frac{1}{2} s_{2\alpha_{hS}}$	0	0
c_{AAVV}	$c_{\alpha_{AS}}^2$	1	1	1	1	$c_{\alpha_{AS}}^2$
$c_{A_S A_S VV}$	$s_{\alpha_{AS}}^2$	0	0	0	0	$s_{\alpha_{AS}}^2$
$c_{A A_S VV}$	$-\frac{1}{2} s_{2\alpha_{AS}}$	0	0	0	0	$-\frac{1}{2} s_{2\alpha_{AS}}$
$c_{H^\pm H^\mp Z}$		1	1	1	1	1
$c_{H^\pm H^\mp \gamma}$		1	1	1	1	1
$c_{H^\pm H^\mp VV}$		1	1	1	1	1
Relevant mixing		—	H, h	h, h_S	H, h_S	A, A_S

Table 2. The couplings between Higgs bosons and gauge bosons in 2HDM+S.

the quartic coupling $HhVV$ is zero for the benchmark cases as well, and is non-zero only when α_{HS} and α_{hS} are both non-zero.

3 Oblique parameters

Since the oblique parameters STU are constructed with the W and Z self-energies [16], as shown in Eqs. (A.2)-(A.3), they receive contributions from the Feynman Diagrams in Fig. 1.

The three-point vertices (including $h_i VV$, $h_i a_j Z$, $h_i/a_i H^\pm W^\mp$ and $Z/\gamma H^\pm H^\mp$), as well as the four-point vertices (including $h_i h_i VV$, $a_i a_i VV$ and $H^\pm H^\mp VV$), contribute to the gauge bosons self-energies.

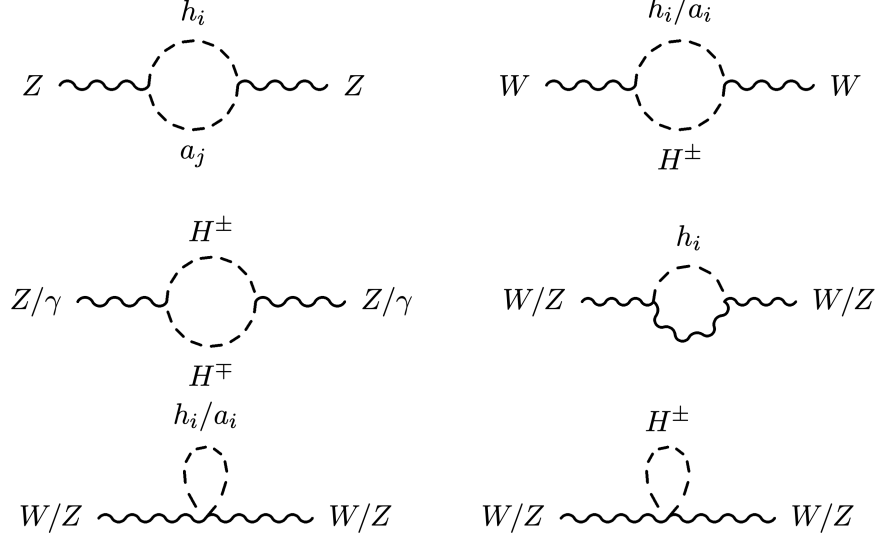


Figure 1. Feynman diagrams that contribute to the self energy of the SM gauge bosons.

The contributions to the STU parameters from various Higgses can be found in Ref. [17]. Using those expressions, the STU parameters in 2HDM+S are given by

$$\begin{aligned}
S = & \frac{1}{24\pi} \left[(2s_W^2 - 1)^2 G(m_{H^\pm}^2, m_{H^\pm}^2, m_Z^2) + \sum_{i,j} |c_{a_i h_j Z}|^2 G(m_{a_i}^2, m_{h_j}^2, m_Z^2) \right. \\
& + \sum_{i=1}^3 c_{h_i h_i VV} \ln(m_{h_i}^2) + \sum_{i=1}^2 c_{a_i a_i VV} \ln(m_{a_i}^2) - 2 \ln(m_{H^\pm}^2) - \ln(m_{h_{\text{ref}}}^2) \\
& \left. + \sum_{i=1}^3 |c_{h_i VV}|^2 \hat{G}(m_{h_i}^2, m_Z^2) - \hat{G}(m_{h_{\text{ref}}}^2, m_Z^2) \right], \tag{3.1}
\end{aligned}$$

$$\begin{aligned}
T = & \frac{1}{16\pi s_W^2 m_W^2} \left[\sum_{i=1}^3 |c_{h_i H^\pm W^\mp}|^2 F(m_{H^\pm}^2, m_{h_i}^2) + \sum_{i=1}^2 |c_{a_i H^\pm W^\mp}|^2 F(m_{H^\pm}^2, m_{a_i}^2) \right. \\
& - \sum_{i,j} |c_{a_i h_j Z}|^2 F(m_{a_i}^2, m_{h_j}^2) + 3 \sum_{i=1}^3 |c_{h_i VV}|^2 (F(m_Z^2, m_{h_i}^2) - F(m_W^2, m_{h_i}^2)) \\
& \left. - 3 (F(m_Z^2, m_{h_{\text{ref}}}^2) - F(m_W^2, m_{h_{\text{ref}}}^2)) \right], \tag{3.2}
\end{aligned}$$

$$\begin{aligned}
U = & \frac{1}{24\pi} \left[\sum_{i=1}^3 |c_{h_i H^\pm W^\mp}|^2 G(m_{H^\pm}^2, m_{h_i}^2, m_W^2) + \sum_{i=1}^2 |c_{a_i H^\pm W^\mp}|^2 G(m_{H^\pm}^2, m_{a_i}^2, m_W^2) \right. \\
& - (2s_W^2 - 1)^2 G(m_{H^\pm}^2, m_{H^\pm}^2, m_Z^2) - \sum_{i,j} |c_{a_i h_j Z}|^2 G(m_{a_i}^2, m_{h_j}^2, m_Z^2) \\
& \left. + \sum_{i=1}^3 |c_{h_i VV}|^2 \left(\hat{G}(m_{h_i}^2, m_W^2) - \hat{G}(m_{h_i}^2, m_Z^2) \right) - \hat{G}(m_{h_{\text{ref}}}^2, m_W^2) + \hat{G}(m_{h_{\text{ref}}}^2, m_Z^2) \right], \quad (3.3)
\end{aligned}$$

where the $m_{h_{\text{ref}}} = 125$ GeV is the reference mass of the SM Higgs. Functions F , G and \hat{G} can be found in Eqs. (A.4), (A.5) and (A.6) in Appendix A.

For the T parameter, the contributions from the quartic couplings cancel, since $\varphi_i \varphi_i WW$ are the same as $\varphi_i \varphi_i ZZ$ and T observable is defined by the self-energy difference between W boson and Z boson (see Eq. (A.1)). Thus, the T observable only receives the contribution from the $h_i VV$, $a_i h_j Z$ and $a_i/h_i H^\pm W^\mp$ couplings. Furthermore, the S parameter mainly represents the Z boson self-energy, and receives contributions from the $ZH^\pm H^\mp$ interaction via $G(m_{H^\pm}^2, m_{H^\pm}^2, m_Z^2)$ and the $a_i h_j Z$ interaction via $G(m_{a_i}^2, m_{h_j}^2, m_Z^2)$. In addition, the quartic couplings $h_i h_i VV$, $a_i a_i VV$ and $H^\pm H^\pm VV$ enter into the S parameter via the logarithmic functions. For the U parameter, the contributions of the quartic interactions cancel again. Furthermore, the U parameter is related to the dim-8 operator, which is usually suppressed. Therefore, in our discussion below, we mostly focus on the S and T parameters, which are more sensitive to the BSM effects.

The experimental measurements for the electroweak precision observables yield the following best-fit values of STU [19] for $m_{h_{\text{ref}}} = 125$ GeV:

$$\begin{aligned}
S^{\text{exp}} &= -0.04, & T^{\text{exp}} &= 0.01, & U^{\text{exp}} &= -0.01, \\
\Delta S &= 0.10, & \Delta T &= 0.12, & \Delta U &= 0.09, \\
\text{corr}(S, T) &= +0.93, & \text{corr}(S, U) &= -0.70, & \text{corr}(T, U) &= -0.87,
\end{aligned} \quad (3.4)$$

where $\text{corr}(S, T)$, $\text{corr}(S, U)$ and $\text{corr}(T, U)$ are the correlation coefficients between the S , T and U . The contributions to the oblique parameters STU in 2HDM+S, i.e., Eqs. (3.2), (3.1) and (3.3), can be used to construct the χ^2 value [18, 20],

$$\chi_{STU}^2 = \left(S - S^{\text{exp}}, T - T^{\text{exp}}, U - U^{\text{exp}} \right) \cdot \mathbf{cov}^{-1} \cdot \begin{pmatrix} S - S^{\text{exp}} \\ T - T^{\text{exp}} \\ U - U^{\text{exp}} \end{pmatrix}, \quad (3.5)$$

where

$$\mathbf{cov} = \begin{pmatrix} \Delta S^2 & \text{corr}(S, T) \Delta S \Delta T & \text{corr}(S, U) \Delta S \Delta U \\ \text{corr}(S, T) \Delta S \Delta T & \Delta T^2 & \text{corr}(T, U) \Delta T \Delta U \\ \text{corr}(S, U) \Delta S \Delta U & \text{corr}(T, U) \Delta T \Delta U & \Delta U^2 \end{pmatrix}. \quad (3.6)$$

The two-dimensional fit to the STU parameters at 95% C.L. corresponds to $\Delta\chi^2 = \chi_{STU}^2 - \chi_{STU}^2|_{\text{minimal}} < 5.99$.

4 Five Benchmark Cases

In the 2HDM, the STU parameters play an important role in constraining the mass splittings between the BSM neutral Higgses and the charged Higgses H^\pm . In 2HDM+S, the singlet field enters via the mixing, which further changes the dependence of the STU parameters on model parameters. In this section, we explore the impacts of electroweak constraints on the mixing angles, $\beta - \alpha$, α_{h_S} , α_{H_S} , and α_{A_S} , as well as various mass splittings. For convenience, we define the following mass splittings, which are relevant for the STU constraints,

$$\begin{aligned}\Delta m_H &= m_H - m_{H^\pm}, & \Delta m_A &= m_A - m_{H^\pm}, \\ \Delta m_{h_S} &= m_{h_S} - m_{H^\pm}, & \Delta m_{A_S} &= m_{A_S} - m_{H^\pm}.\end{aligned}\tag{4.1}$$

4.1 Case-0

As a starting point, we study the simplest Case-0 (the 2HDM alignment limit) with $c_{\beta-\alpha} = \alpha_{H_S} = \alpha_{h_S} = \alpha_{A_S} = 0$. According to Table 2, the non-zero couplings in this case are

$$c_{hVV}, c_{AHZ}, c_{HH^\pm W^\mp}, c_{AH^\pm W^\mp}, c_{ZH^\pm H^\mp}, c_{hhVV}, c_{HHVV}, c_{AAVV}, c_{H^\pm H^\mp VV},\tag{4.2}$$

with norm 1. The 125 GeV Higgs h is the SM Higgs and singlet Higgs bosons h_S and A_S both decouple. The doublet BSM Higgses H , A and H^\pm enter via AHZ , $HH^\pm W^\mp$ and $AH^\pm W^\mp$ interactions and mainly contribute to the terms involving F functions in the T parameter. In addition, $ZH^\pm H^\mp$ and quartic interactions $HHVV$, $AAVV$ and $H^\pm H^\mp VV$ contribute to the S parameter. Consequently, the masses of H , A and H^\pm are relevant for the oblique parameters, while the singlet Higgs masses m_{h_S} and m_{A_S} are irrelevant.

The T and S parameters in this case, denoted as T_0 and S_0 , are given by [20]

$$\begin{aligned}T_0 &= \frac{1}{16\pi s_W^2 m_W^2} [F(m_{H^\pm}^2, m_H^2) - F(m_A^2, m_H^2) + F(m_{H^\pm}^2, m_A^2)], \\ S_0 &= \frac{1}{24\pi} [(2s_W^2 - 1)^2 G(m_{H^\pm}^2, m_{H^\pm}^2, m_Z^2) + G(m_A^2, m_H^2, m_Z^2) + \ln\left(\frac{m_H^2}{m_{H^\pm}^2}\right) + \ln\left(\frac{m_A^2}{m_{H^\pm}^2}\right)],\end{aligned}\tag{4.3}$$

$$\tag{4.4}$$

The values of T_0 with varying Δm_H and Δm_A are presented by the solid lines in Fig. 2. The left panel is for varying Δm_H with fixed $\Delta m_A = 0, \pm 50$ GeV, and the right panel is for varying Δm_A with fixed $\Delta m_H = 0, \pm 50$ GeV. As indicated by Eq. (4.3), T_0 is exactly zero when $\Delta m_H = 0$ or $\Delta m_A = 0$. The grey hatch area is the 1σ region of the electroweak precision observable fit to the T parameter. T_0 is also symmetric under the exchange of m_H and m_A . Therefore, the T_0 dependence on Δm_H in the left panel is the same as the T_0 dependence on Δm_A in the right panel. T_0 increases as Δm_H (Δm_A) increases for $\Delta m_A > 0$ ($\Delta m_H > 0$), while decreases for the opposite sign of Δm_A (Δm_H). Furthermore, $T_0 > 0$ when both Δm_H and Δm_A have the same sign, and $T_0 < 0$ when Δm_H and Δm_A have the opposite signs.

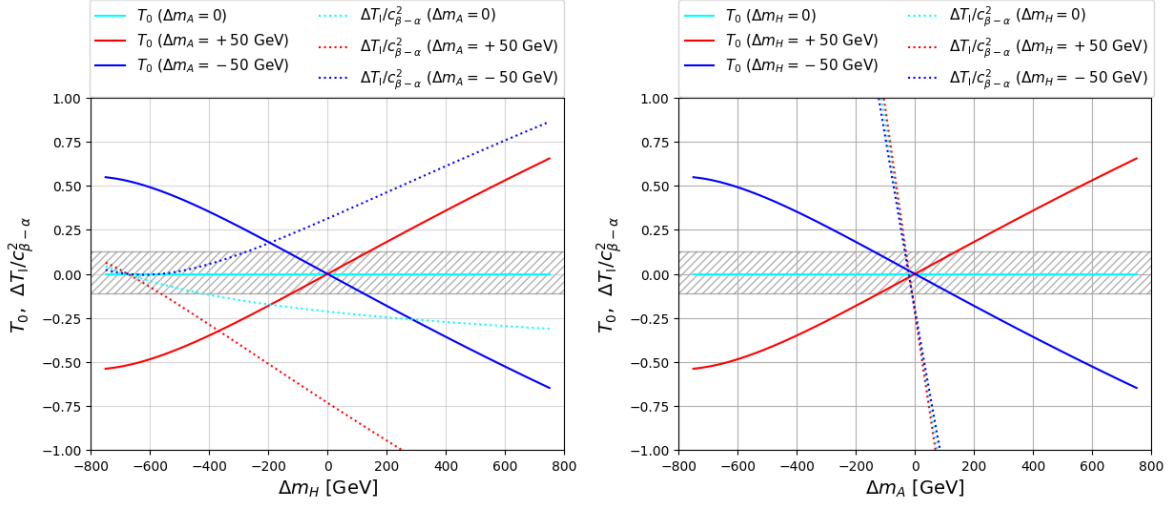


Figure 2. T_0 (solid lines) and $\Delta T_1/c_{\beta-\alpha}^2$ (dotted lines) with varying Δm_H (left) and Δm_A (right). Cyan, red, and blue lines are for $\Delta m_{A,H} = 0, +50$ GeV and -50 GeV, respectively. The grey hatch area is the 1σ region of the T observable. m_{H^\pm} is chosen to be 800 GeV.

The S_0 parameter, however, is not zero even when both Δm_A and Δm_H are zero. The contributions from $G(m_i^2, m_j^2, m_k^2)$, however, are typically very small. The main contributions to S_0 come from the logarithmic terms $\ln(m_{H,A}^2/m_{H^\pm}^2)$. For $\Delta m_{H,A}$ in the range of ± 700 GeV, $|S_0| < 0.15$ is within 1σ range of the fitted value.

Fig. 3 shows the 95% C.L. allowed region from the STU constrains in the Δm_H vs. Δm_A plane. The blue region corresponds to the Case-0 with $c_{\beta-\alpha} = \alpha_{HS} = \alpha_{hS} = \alpha_{AS} = 0$ and $m_{H^\pm} = 800$ GeV, which centers around $\Delta m_H = 0$ or $\Delta m_A = 0$. Due to the positive correlation between S and T observables, the area with positive T is preferred. Therefore, the allowed regions with the same signs of Δm_A and Δm_H are bigger comparing to the allowed regions with the opposite signs.

In Figs. 4, the 95% C.L. allowed regions under the STU constraints are shown in the $\Delta m_{A,H}$ vs. $c_{\beta-\alpha}$ plane. For $c_{\beta-\alpha} = 0$, the 95% C.L. fit to the STU parameters gives $\Delta m_{A,H} \lesssim 900$ GeV with $\Delta m_{H,A} = 0$ for $m_{H^\pm} = 800$ GeV (blue region). The upper limits on $\Delta m_{A,H}$ come from the logarithm contributions. These upper limits of $\Delta m_{A,H}$ vary with the benchmark value of m_{H^\pm} and increase as H^\pm becomes heavier, as indicated by the green dashed curve for $m_{H^\pm} = 1000$ GeV. For non-zero values of $\Delta m_{A,H} = \pm 50$ GeV, the allowed range of $\Delta m_{H,A}$ is much smaller, as shown by the regions with the purple and orange boundary curves in Figs. 4.

4.2 Case-I: $c_{\beta-\alpha} \neq 0$

In the Case-I ($c_{\beta-\alpha} \neq 0$ and $\alpha_{HS} = \alpha_{hS} = \alpha_{AS} = 0$), the singlet fields decouple completely, and the model is the same as the 2HDM. In particular, we have the following non-zero

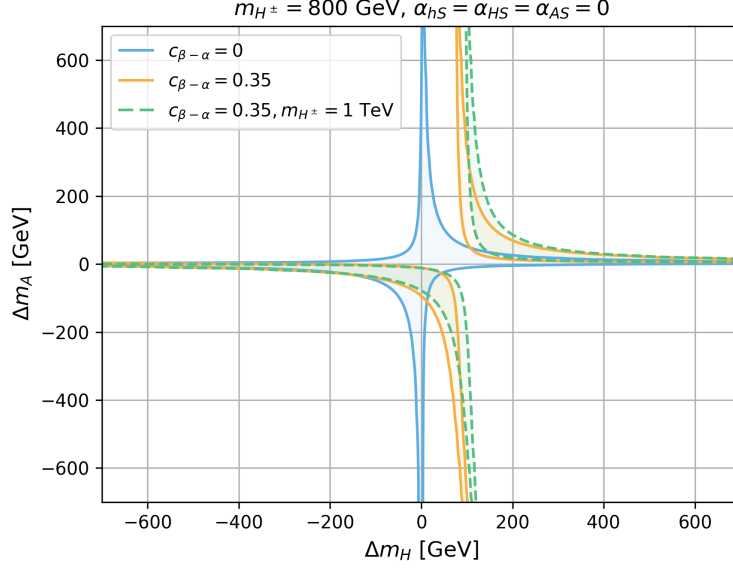


Figure 3. The 95% C.L. allowed region from *STU* constraints in the plane Δm_H vs. Δm_A with $c_{\beta-\alpha} = 0$ (solid blue region) and 0.35 (solid orange region) for $m_{H^\pm} = 800$ GeV. The other parameters are $\alpha_{HS} = \alpha_{hS} = \alpha_{AS} = 0$. For $m_{H^\pm} = 1000$ GeV, the allowed region for $c_{\beta-\alpha} = 0$ is approximately the same to $m_{H^\pm} = 800$ GeV, while the region for $c_{\beta-\alpha} = 0.35$ are shown by the green regions.

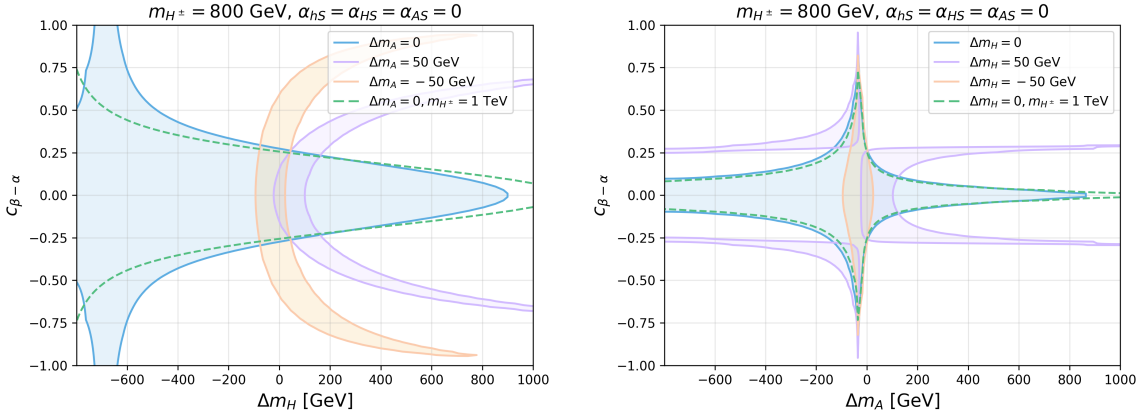


Figure 4. The 95% C.L. allowed region via *STU* constraints on $c_{\beta-\alpha}$ vs. Δm_H (left) and Δm_A vs $c_{\beta-\alpha}$ (right). The other parameters are chosen as $\alpha_{HS} = \alpha_{hS} = \alpha_{AS} = 0$ and $m_{H^\pm}^\pm = 800$ GeV (solid curves). Blue, purple and orange regions correspond to $\Delta m_{A,H} = 0, 50, -50$ GeV, respectively. Green dashed curves are for $m_{H^\pm} = 1000$ GeV and $\Delta m_{A,H} = 0$.

couplings in addition to those shown in Eq. (4.2)

$$c_{HVV}, c_{AhZ}, c_{hH^\pm W^\mp}, \quad (4.5)$$

which are proportional to $c_{\beta-\alpha}$ and provide additional contributions to the STU parameters. Similar to the Case-0, the singlet masses m_{h_S} and m_{A_S} are irrelevant, and only the doublet-like Higgs masses m_H , m_A and m_{H^\pm} enter. The STU constraints of 2HDM have been studied in the literature [18, 21]. The T observable in the Case-I is

$$T_I = T_0 + \Delta T_I \quad (4.6)$$

$$\begin{aligned} \Delta T_I = & \frac{c_{\beta-\alpha}^2}{16\pi s_W^2 m_W^2} \{F(m_h^2, m_{H^\pm}^2) - F(m_h^2, m_A^2) - [F(m_H^2, m_{H^\pm}^2) - F(m_H^2, m_A^2)] \\ & - 3[F(m_h^2, m_Z^2) - F(m_h^2, m_{W^\pm}^2)] + 3[F(m_H^2, m_Z^2) - F(m_H^2, m_{W^\pm}^2)]\}. \end{aligned} \quad (4.7)$$

Comparing to the Case-0, the additional contribution of ΔT_I is proportional to $c_{\beta-\alpha}$, which is non-zero even for $\Delta m_A = 0$.

In Fig. 2, we show the value of T_0 (solid curves) and $\Delta T_I/c_{\beta-\alpha}^2$ (dashed curves) for different values of Δm_H and Δm_A . The left panel shows that for $\Delta m_H = -675$ GeV, which corresponds to $m_H = m_h = 125$ GeV, $\Delta T_I = 0$. Right panel shows that ΔT_I has the opposite (same) sign of T_0 for positive (negative) Δm_H , except for a small negative Δm_A region.

The 95% C.L. STU allowed parameter space in Δm_H vs Δm_A plane are shown in Fig. 3 for $c_{\beta-\alpha} = 0.35$ (orange). The allowed regions shift to the right ($\Delta m_H > 0$), given the cancellation between T_0 and ΔT_I . In particular, the $\Delta m_A = 0$ point with $\Delta m_H \sim 100$ GeV and $c_{\beta-\alpha} = 0.35$ would be excluded, since T_0 is zero and cannot eliminate the non-zero ΔT_I . The regions enclosed by the green dashed curves are for $m_{H^\pm} = 1000$ GeV, which is close to the orange regions of $m_{H^\pm} = 800$ GeV.

Left panel of Fig. 4 shows the 95% C.L. STU allowed parameter space in $c_{\beta-\alpha}$ vs Δm_H for various Δm_A . The allowed regions are symmetric with respect to $c_{\beta-\alpha} = 0$ given the $c_{\beta-\alpha}^2$ dependence. For $\Delta m_A = 0$ (region enclosed by the solid blue curve), all values of $c_{\beta-\alpha}$ is allowed at $m_H = 125$ GeV: $T_0 = 0$ since $\Delta m_A = 0$, and $\Delta T_I = 0$ for $m_H = m_h = 125$ GeV. The allowed regions shrink for larger $|m_H - m_{h_{125}}|$. The green dashed line indicates the impact of the value of $m_{H^\pm}^\pm$. For non-zero Δm_A , the non-zero T_0 could be canceled by ΔT_I . The allowed regions favor mostly positive Δm_H , as shown by the regions enclosed by the purple curves and orange curves. Since the absolute value of ΔT_I is larger when Δm_A is positive as shown in Fig. 2, the allowed regions with positive Δm_A favor smaller $|c_{\beta-\alpha}|$. The 2HDM non-alignment case has been studied in [21], which did not cover the case with much larger mass splittings.

The right panel of Fig. 4 shows the 95% C.L. STU allowed parameter space in $c_{\beta-\alpha}$ vs Δm_A for various Δm_H . For $\Delta m_H = 0$ (region enclosed by the solid blue curves), relatively large region of $c_{\beta-\alpha}$ is allowed for $\Delta m_A \sim -30$ GeV, when $\Delta T_I \sim 0$ and S_0 and T_0 are small. The allowed regions of $c_{\beta-\alpha}$ are smaller for $\Delta m_A > 0$ comparing to $\Delta m_A < 0$, since $|\Delta T_I|$ is larger for positive Δm_A . Also note that for negative $\Delta m_H = -50$ GeV, only a narrow range of Δm_A around -30 GeV is allowed. This is because ΔT_I has the same signs as T_0 for negative Δm_H . Therefore, only small values of Δm_A are allowed. However, for positive $\Delta m_H = 50$

GeV, ΔT_I and T_0 have opposite signs. A wide range of Δm_A is allowed: $|c_{\beta-\alpha}| \lesssim 0.25$ for $\Delta m_A > 0$, and $|c_{\beta-\alpha}| \gtrsim 0.25$ for $\Delta m_A < 0$.

4.3 Case-II: $\alpha_{h_S} \neq 0$

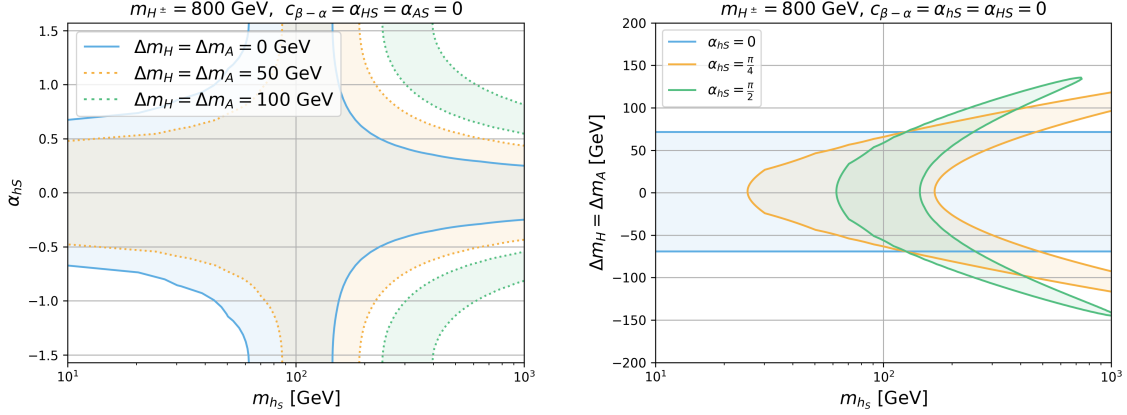


Figure 5. 95% C.L. STU constraints on the parameter space of m_{h_S} , α_{h_S} and Δm_A . The left panel is for m_{h_S} vs α_{h_S} with varying Δm_A . The blue, orange and green regions are for $\Delta m_A = \Delta m_H = 0, 50, 100$ GeV, respectively. The right panel is for m_{h_S} vs $\Delta m_{H,A}$ with varying α_{h_S} . The blue, orange and green regions are for $\alpha_{h_S} = 0, \frac{\pi}{4}$ and $\frac{\pi}{2}$, respectively. For both panel, we set $m_{H^\pm} = 800$ GeV and $c_{\beta-\alpha} = \alpha_{HS} = \alpha_{AS} = 0$.

In the Case-II (e.g. $\alpha_{h_S} \neq 0$ and $c_{\beta-\alpha} = \alpha_{HS} = \alpha_{AS} = 0$), the 125 GeV Higgs h mixes with the singlet-like Higgs h_S , and the $h_S VV$ coupling is proportional to $s_{\alpha_{h_S}}$, which is the only non-zero trilinear coupling between Higgs and gauge bosons, in addition to those in Eq. (4.2). The $Ah_S Z$ and $h_S H^\pm W^\mp$ couplings are still zero, which means α_{h_S} cannot connect the h_S with the BSM doublet-like Higgses H, A or H^\pm . This case is similar to the singlet extension of the SM (SSM), where the singlet Higgs only mixes with the SM Higgs h . Therefore, the STU parameters receive additional contribution via loops with $h_S VV$ vertices, with the singlet Higgs mass m_{h_S} entering. The S and T parameters are given by

$$S_{\text{II}} = S_0 + \Delta S_{\text{II}}, \quad T_{\text{II}} = T_0 + \Delta T_{\text{II}}, \quad (4.8)$$

$$\Delta S_{\text{II}} = \frac{1}{24\pi} s_{\alpha_{h_S}}^2 \left[\ln \left(\frac{m_{h_S}^2}{m_{h_{125}}^2} \right) + \hat{G}(m_{h_S}^2, m_Z^2) - \hat{G}(m_{h_{125}}^2, m_Z^2) \right], \quad (4.9)$$

$$\Delta T_{\text{II}} = \frac{1}{16\pi s_W^2 m_W^2} 3s_{\alpha_{h_S}}^2 \left[F(m_Z^2, m_{h_S}^2) - F(m_W^2, m_{h_S}^2) - F(m_Z^2, m_{h_{125}}^2) + F(m_W^2, m_{h_{125}}^2) \right] \quad (4.10)$$

The expression for the function \hat{G} can be found in Eq. (A.6). Note that ΔT_{II} and ΔS_{II} are proportional to $s_{\alpha_{h_S}}^2$, and both terms vanish when $m_{h_S} = m_{h_{125}}$. ΔS_{II} is in general suppressed,

while ΔT_{II} could receive significant contribution when m_{h_S} is away from 125 GeV, which is negative (positive) for $m_{h_S} > (<) 125$ GeV. Meanwhile, the masses of H , A or H^\pm can still contribute via T_0 and S_0 .

In the left panel of Fig. 5, we show the 95% C.L. allowed region from the STU constraints in m_{h_S} vs α_{h_S} plane for different values of $\Delta m_H = \Delta m_A$. For $\Delta m_H = \Delta m_A = 0$ (blue), all values of α_{h_S} are allowed for $m_{h_S} = m_h \approx 125$ GeV. The allowed region for α_{h_S} reduces for m_{h_S} away from 125 GeV: $|\alpha_{h_S}| \lesssim 0.7$ for light $m_{h_S} = 10$ GeV and $|\alpha_{h_S}| \lesssim 0.2$ for $m_{h_S} = 1$ TeV.

For $\Delta m_H = \Delta m_A = 50$ GeV (orange), the 95% C.L. allowed region shifted to right of $m_{h_S} = 125$ GeV, due to the opposite signs of T_0 and ΔT_{II} for $m_{h_S} > 125$ GeV. For $\Delta m_H = \Delta m_A = 100$ GeV (green), T_0 is so large that only two thin branches in $m_{h_S} > 240$ GeV and $0.5 < |\alpha_{h_S}| < \pi/2$ are allowed.

In the right panel of Fig. 5, we show the 95% C.L. STU allowed region in m_{h_S} vs $\Delta m_{H,A}$ plane for $\alpha_{h_S} = 0$ (blue), $\pi/4$ (orange) and $\pi/2$ (green). For $\alpha_{h_S} = 0$, the bound of $|\Delta m_H| = |\Delta m_A| \lesssim 80$ GeV is independent of m_{h_S} . For non-zero α_{h_S} , the allowed value in $|\Delta m_{H,A}|$ reduces for $m_{h_S} < 125$ GeV, while increases for $m_{h_S} > 125$ GeV. Note that all curves cross at $m_{h_S} = 125$ GeV since ΔT_{II} and ΔS_{II} vanish at $m_{h_S} = 125$ GeV regardless of the value of α_{h_S} . There is a slight asymmetry between the positive and negative values of $\Delta m_H = \Delta m_A$. This is because S_0 observable is not symmetric between positive and negative $\Delta m_{H,A}$. ΔS_{II} is always positive for $m_{h_S} > m_{h_{125}}$ while the sign of S_0 flips for different sign of $\Delta m_{H,A}$. Therefore, the S observable is larger for positive $\Delta m_{H,A}$ and the constraint would be stronger, which leads to slightly smaller allowed region for $\Delta m_{H,A} > 0$ comparing to the negative mass difference case.

4.4 Case-III: $\alpha_{HS} \neq 0$

The Case-III corresponds to $\alpha_{HS} \neq 0$ and $c_{\beta-\alpha} = \alpha_{h_S} = \alpha_{AS} = 0$, when h_S mixes with the doublet-like CP-even Higgs H . The non-zero trilinear Higgs to gauge-boson couplings include

$$c_{Ah_S Z}, c_{h_S H^\pm W^\mp}, \quad (4.11)$$

in addition to those in Eq. (4.2). The $h_S VV$ coupling, however, remains to be zero in this case. While the additional contribution to the S observable is small, the T observable could receive significant contributions:

$$T = \frac{1}{16\pi s_W^2 m_W^2} [c_{\alpha_{HS}}^2 F(m_{H^\pm}^2, m_H^2) + s_{\alpha_{HS}}^2 F(m_{H^\pm}^2, m_{h_S}^2)] \\ + F(m_{H^\pm}^2, m_A^2) - [c_{\alpha_{HS}}^2 F(m_A^2, m_H^2) + s_{\alpha_{HS}}^2 F(m_A^2, m_{h_S}^2)]. \quad (4.12)$$

$$= T_0 + \Delta T_{\text{III}}, \quad (4.13)$$

$$\Delta T_{\text{III}} = \frac{s_{\alpha_{HS}}^2}{16\pi s_W^2 m_W^2} [F(m_{H^\pm}^2, m_{h_S}^2) - F(m_A^2, m_{h_S}^2) - F(m_{H^\pm}^2, m_H^2) + F(m_A^2, m_H^2)]. \quad (4.14)$$

In addition to $\Delta m_{H,A}$, $\Delta m_{h_S} = m_{h_S} - m_{H^\pm}$ also enters.

There is a numerical approximation for the F function in Eq. (A.4):

$$\begin{aligned} & c_\alpha^2[F(J^2, I^2) - F(K^2, I^2)] + s_\alpha^2[F(J^2, L^2) - F(K^2, L^2)] \\ & \approx F(J^2, [c_\alpha^2 I + s_\alpha^2 L]^2) - F(K^2, [c_\alpha^2 I + s_\alpha^2 L]^2). \end{aligned} \quad (4.15)$$

Therefore, the T observable can be approximated as

$$T \approx \frac{1}{16\pi s_W^2 m_W^2} [F(m_{H^\pm}^2, (c_{\alpha_{HS}}^2 m_H + s_{\alpha_{HS}}^2 m_{h_S})^2) - F(m_A^2, (c_{\alpha_{HS}}^2 m_H + s_{\alpha_{HS}}^2 m_{h_S})^2) + F(m_{H^\pm}^2, m_A^2)] \quad (4.16)$$

which vanishes for

$$c_{\alpha_{HS}}^2 m_H + s_{\alpha_{HS}}^2 m_{h_S} = m_{H^\pm}, \quad \text{or } m_A = m_{H^\pm}. \quad (4.17)$$

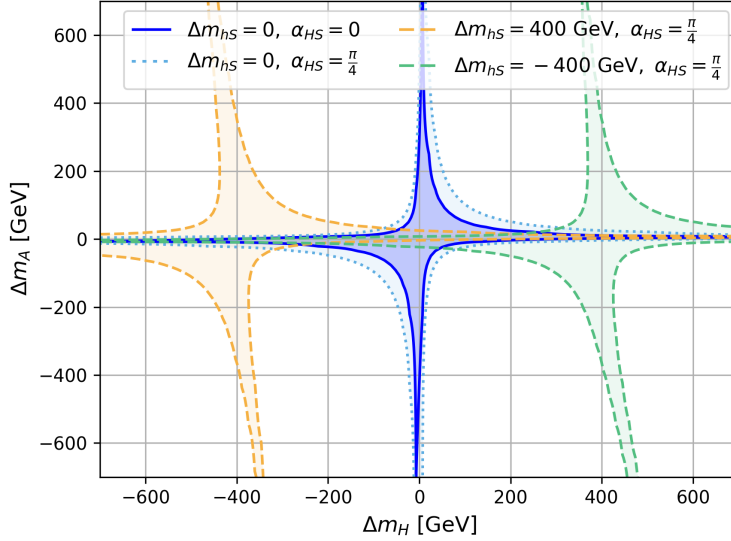


Figure 6. The 95% C.L. STU allowed region in Δm_H vs. Δm_A in the Case-III with $c_{\beta-\alpha} = \alpha_{h_S} = \alpha_{A_S} = 0$. m_{H^\pm} is set to be 800 GeV. Regions enclosed by the dark solid blue and light dashed blue curves are for $\Delta m_{h_S} = 0$ and $\alpha_{HS} = 0$ and $\pi/4$ respectively. Orange and green regions are for $\Delta m_{h_S} = \pm 400$ GeV, respectively, and $\alpha_{HS} = \pi/4$.

Fig. 6 presents the 95% STU allowed region in the Δm_H vs Δm_A plane for the Case-III. The region enclosed by the dark blue curves corresponds to the baseline Case-0 when $\alpha_{HS} = 0$. For $\alpha_{HS} = \pi/4$ and $\Delta m_{h_S} = 0$ (region enclosed by the light dotted blue lines), the 95% C.L. STU allowed region would be slightly enlarged compared to the Case-0 since the mass-splitting effect of H with H^\pm is suppressed by $c_{\alpha_{HS}}^2 = 1/2$, while the h_S has no mass splitting with the charged Higgs, as shown in Eq. (4.17).

When the singlet-like Higgs mass is deviated from the charged Higgs mass, for instance, $\Delta m_{h_S} = \pm 400$ GeV with $\alpha_{HS} = \pi/4$, as shown by the orange and green regions, the central of

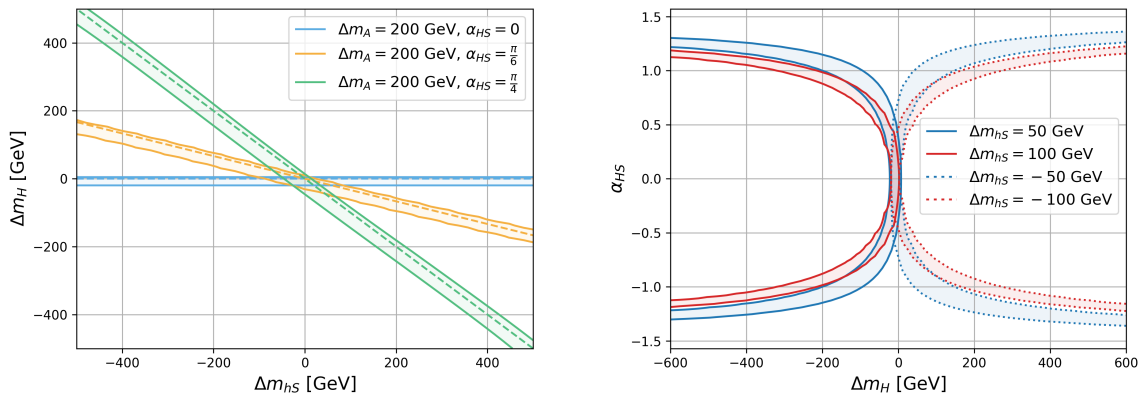


Figure 7. The 95% C.L. *STU* allowed region in Δm_H vs. Δm_{h_S} plane (left panel) and Δm_H vs. α_{HS} plane (right panel) in the Case-III with $c_{\beta-\alpha} = \alpha_{h_S} = \alpha_{A_S} = 0$. In the left panel, α_{HS} is varied to be 0 (blue), $\pi/6$ (orange) and $\pi/4$ (green). In the right panel, Δm_{h_S} is varied to be ± 50 GeV (solid and dashed blue) and ± 100 GeV (solid and dashed red). m_{H^\pm} is set to be 800 GeV and Δm_A is set to be 200 GeV.

the allowed region in Δm_H would be shifted to the region of $\Delta m_H \approx \mp 400$ GeV to satisfy the mass relation in Eq. (4.17) in order to suppress the contributions to the T parameter. Note that $\Delta m_A = 0$ is still allowed, regardless of the choices of Δm_H , Δm_{h_S} and α_{HS} .

In the left panel of Fig. 7, we show the 95% C.L. *STU* allowed region in Δm_H vs. Δm_{h_S} plane in the Case-III for $m_{H^\pm} = 800$ GeV and $\Delta m_A = 200$ GeV, with varying $\alpha_{HS} = 0$ (blue), $\pi/6$ (orange), and $\pi/4$ (green). Also shown in dashed lines are the approximate relation of $c_{\alpha_{HS}}^2 \Delta m_H = -s_{\alpha_{HS}}^2 \Delta m_{h_S}$ based on Eq. (4.17). As the mass splitting Δm_A increases, the *STU* bands would shrink and be closer to the dashed lines.

In the right panel of Fig. 7, we show the 95% C.L. *STU* allowed region in Δm_H vs. α_{HS} plane in the Case-III for $m_{H^\pm} = 800$ GeV and $\Delta m_A = 200$, with varying $\Delta m_{h_S} = \pm 50$ GeV (blue) and 100 GeV (red). Note that the allowed regions are symmetric in α_{HS} and only have slight variation with respect to the sign of Δm_H .

4.5 Case-IV: $\alpha_{A_S} \neq 0$

In the Case-IV, ($\alpha_{A_S} \neq 0$ and $c_{\beta-\alpha} = \alpha_{h_S} = \alpha_{HS} = 0$), the CP-odd sector has singlet admixture and CP-even sector is the same as the Case-0. The non-zero trilinear Higgs to gauge-boson couplings include

$$c_{A_S H Z}, c_{A_S H^\pm W^\mp}, \quad (4.18)$$

in addition to those in Eq. (4.2). Consequently, the couplings involving CP-odd Higgses are parametrized by α_{A_S} , i.e. $AH Z$ and $AH^\pm W^\mp$ depend on $c_{\alpha_{A_S}}$, $A_S H Z$ and $A_S H^\pm W^\mp$ depend on $s_{\alpha_{A_S}}$. The singlet CP-odd Higgs mass m_{A_S} enters while the CP-even h_S is completely

decoupled. In particular, the contributions to the T observable is given by

$$T = \frac{1}{16\pi s_W^2 m_W^2} [c_{\alpha_{AS}}^2 F(m_{H^\pm}^2, m_A^2) + s_{\alpha_{AS}}^2 F(m_{H^\pm}^2, m_{A_S}^2)] \\ + F(m_{H^\pm}^2, m_H^2) - [c_{\alpha_{AS}}^2 F(m_H^2, m_A^2) + s_{\alpha_{AS}}^2 F(m_H^2, m_{A_S}^2)], \quad (4.19)$$

$$= T_0 + \Delta T_{\text{IV}} \quad (4.20)$$

$$\Delta T_{\text{IV}} = \frac{s_{\alpha_{AS}}^2}{16\pi s_W^2 m_W^2} [F(m_{H^\pm}^2, m_{A_S}^2) - F(m_H^2, m_{A_S}^2) - F(m_{H^\pm}^2, m_A^2) + F(m_A^2, m_H^2)] \quad (4.21)$$

Comparing to Eqs. (4.12) and (4.14), we see that the Case-IV is very similar to the Case-III, with the substitution of H and h_S with A and A_S , as well as the corresponding mass parameters and mixing angles. The approximate expression for T is

$$T \approx \frac{1}{16\pi s_W^2 m_W^2} [F(m_{H^\pm}^2, (c_{\alpha_{AS}}^2 m_A + s_{\alpha_{AS}}^2 m_{A_S})^2) - F(m_H^2, (c_{\alpha_{AS}}^2 m_A + s_{\alpha_{AS}}^2 m_{A_S})^2) + F(m_{H^\pm}^2, m_H^2)], \quad (4.22)$$

which leads to a similar approximate mass relation that satisfies the STU constraints:

$$c_{\alpha_{AS}}^2 m_A + s_{\alpha_{AS}}^2 m_{A_S} = m_{H^\pm}, \quad \text{or } m_H = m_{H^\pm}. \quad (4.23)$$

The 95% C.L. STU allowed regions in Δm_H vs. Δm_A , Δm_{A_S} vs. Δm_A , and Δm_A vs. α_{AS} are very similar to those presented in Fig. 6–Fig. 7, with the switching of $A \leftrightarrow H$.

In general, the mass splittings of Δm_H and Δm_A can contribute the STU observables via the AHZ , $AH^\pm W^\mp$ and $HH^\pm W^\mp$ loops. In the 2HDM+S, the singlet CP-even Higgs h_S can mix with H via the mixing α_{HS} , and the singlet CP-odd Higgs A_S can mix with A via α_{AS} . Therefore, Δm_{h_S} , Δm_{A_S} , as well as α_{HS} and α_{AS} enter. The STU constraints can be still fulfilled when the mass relations in Eqs. (4.17) or (4.23) are satisfied.

5 The STU constraints beyond the alignment limit

For the Case-I, we consider the non-alignment limit with all the single mixing angles set to be zero. For the Case-II – IV, we focus on the scenario with only one mixing angle is set to be non-zero under the alignment limit. In this section, we consider the cases with a non-zero singlet mixing angle beyond the alignment limit.

We first explore the interplay between $c_{\beta-\alpha}$ with the singlet– h_{125} mixing α_{h_S} . In the left plot of Fig. 8, we show the 95% C.L. STU allowed region in m_{h_S} vs. $c_{\beta-\alpha}$ plane for various α_{h_S} . For $\alpha_{h_S} = 0$ (region enclosed by the solid blue curve), $|c_{\beta-\alpha}|$ is constrained to be less than 0.275, independent of m_{h_S} . However, the singlet admixture can enlarge the allowed region in $|c_{\beta-\alpha}|$, as shown by the two elliptical rings for $\alpha_{h_S} = \pi/4$ and $\pi/2$. $h_S VV$ interaction can compensate the contribution of ΔT_{I} in. Eq. (4.7) for larger $|c_{\beta-\alpha}|$.

In the right plot of Fig. 8, we present the 95% C.L. STU allowed region in m_{h_S} vs. α_{h_S} plane for various $c_{\beta-\alpha}$. For increasing $|c_{\beta-\alpha}|$, the allowed region shifts to the left. For $m_{h_S} > 125$ GeV, the allowed range of α_{h_S} reduces, while for $m_{h_S} < 125$ GeV, larger values

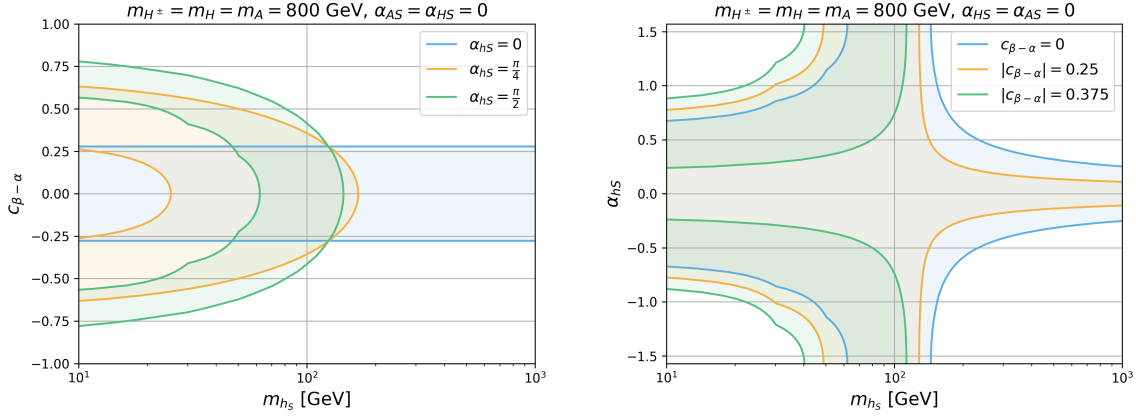


Figure 8. 95% C.L. *STU* allowed region in m_{h_S} vs. $c_{\beta-\alpha}$ plane (left panel) for various $\alpha_{h_S} = 0$ (blue), $\pi/4$ (orange) $\pi/2$ (green), and m_{h_S} vs. α_{h_S} plane (right panel) for various $c_{\beta-\alpha} = 0$ (blue), 0.25 (orange) and 0.375 (green). We set $m_{H^\pm} = m_H = m_A = 800$ GeV and $\alpha_{A_S} = \alpha_{H_S} = 0$.

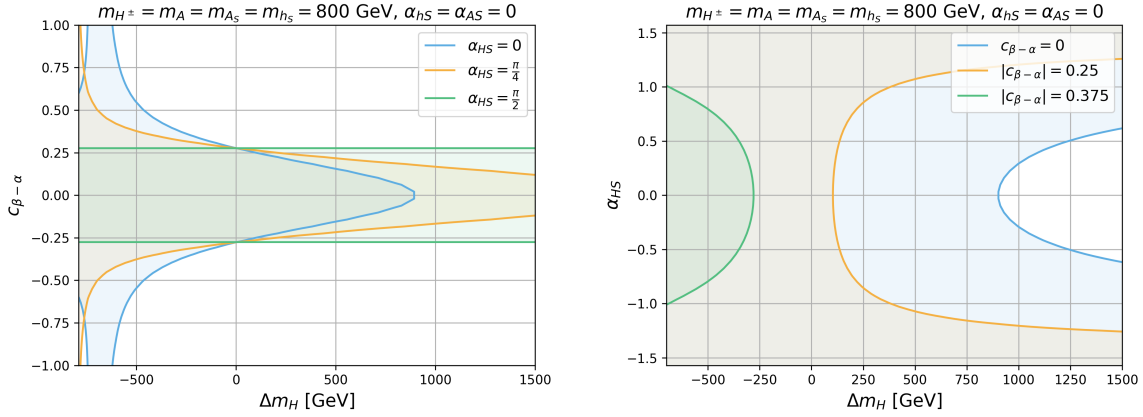


Figure 9. 95% C.L. *STU* allowed region in Δm_H vs. $c_{\beta-\alpha}$ plane (left panel) for various $\alpha_{H_S} = 0$ (blue), $\pi/4$ (orange), $\pi/2$ (green), and Δm_H vs. α_{H_S} plane (right panel) for various $|c_{\beta-\alpha}| = 0$ (blue), 0.25 (orange) and 0.375 (green). We set $m_{H^\pm} = m_A = m_{h_S} = m_{A_S} = 800$ GeV and $\alpha_{A_S} = \alpha_{h_S} = 0$.

of α_{h_S} are allowed. For $|c_{\beta-\alpha}|$ slightly above 0.275, $\alpha_{h_S} = 0$ is no longer allowed, and two branches appear.

We explore the interplay between $c_{\beta-\alpha}$ and singlet-double CP-even Higgs H mixing α_{H_S} in Fig. 9. Left Panel show the 95% C.L. *STU* allowed region in Δm_H vs. $c_{\beta-\alpha}$ plane for $\alpha_{H_S} = 0$ (blue), $\pi/4$ (orange), and $\pi/2$ (green). The blue line in the left panel of Fig. 9 is consistent with the blue curve in the left panel of Fig. 4 (Case-I). For larger α_{H_S} , the allowed range of $c_{\beta-\alpha}$ shrinks for $\Delta m_H < 0$ while expands for $\Delta m_H > 0$. In this case, $c_{HV V} = c_{\beta-\alpha} c_{\alpha_{H_S}}$, $c_{hV V} = s_{\beta-\alpha}$ and $c_{h_S V V} = -c_{\beta-\alpha} s_{\alpha_{H_S}}$. As α_{H_S} increases, the *HVV*

contribution to T observable decreases, while $h_S VV$ contribution increases. Therefore, the allowed $c_{\beta-\alpha}$ region shrinks in the $h_S VV$ dominate region ($m_H < m_{h_S}$) and enlarges in the HVV dominate region ($m_H > m_{h_S}$). When $m_H = m_{h_S} = 800$ GeV, the $h_S VV$ term plays the same role as HVV . The STU constraints of this point are independent of α_{HS} and all curves cross at $\Delta m_H = 0$. For $\alpha_{HS} = \frac{\pi}{2}$, H becomes the pure singlet Higgs and does not contribute to the STU parameters. Therefore, the STU limit of $|c_{\beta-\alpha}| < 0.275$ is independent of m_H . Since the role of H and h_S switches when $\alpha_{HS} \rightarrow \pi/2 - \alpha_{HS}$, the parameter space of $c_{\beta-\alpha}$ vs Δm_{h_S} is the same as the left panel of Fig. 9 with $\alpha_{HS} \rightarrow \pi/2 - \alpha_{HS}$.

The right panel of Fig. 9 presents the Δm_H vs. α_{HS} plane for $|c_{\beta-\alpha}|=0$ (blue), 0.25 (orange) and 0.375 (green). For $c_{\beta-\alpha} = 0$, almost the entire region of parameter space is allowed, except for a small open region with relatively small α_{HS} and large Δm_H . The allowed region reduces when $|c_{\beta-\alpha}|$ increases. For $|c_{\beta-\alpha}| = 0.375$, only a small region with $\Delta m_H < -250$ GeV and $|\alpha_{HS}| < 1$ is allowed. This is due to the increased contribution from HVV term at larger $|c_{\beta-\alpha}| = 0.375$. Only when the m_H is lighter and close to 125 GeV, the HVV contribution would be small enough to be allowed. Similar to the left panel, the parameter space of α_{HS} vs Δm_{h_S} is the same as the right panel of Fig. 9 with $\alpha_{HS} \rightarrow \pi/2 - \alpha_{HS}$.

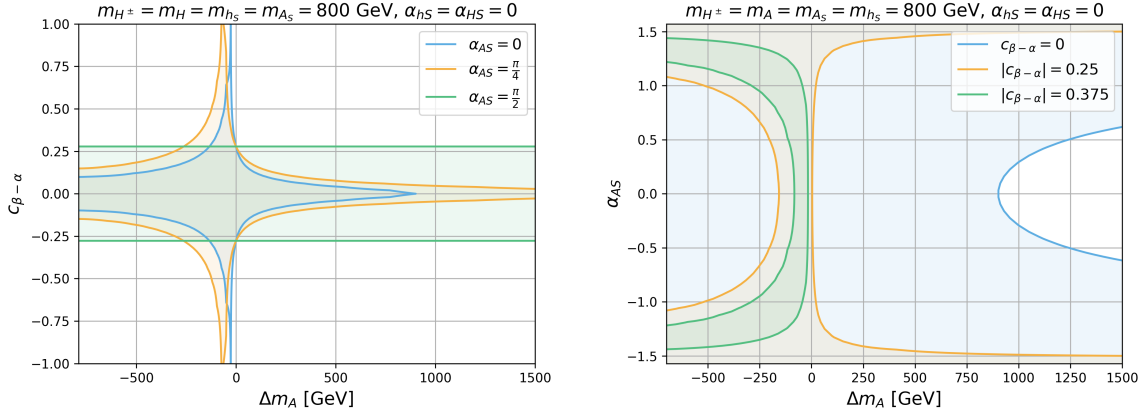


Figure 10. 95% C.L. STU allowed region in Δm_A vs. $c_{\beta-\alpha}$ plane (left panel) for various $\alpha_{HS}=0$ (blue), $\pi/4$ (orange), $\pi/2$ (green), and Δm_A vs. α_{AS} plane (right panel) for various $|c_{\beta-\alpha}|=0$ (blue), 0.25 (orange) and 0.375 (green). We set $m_{H^\pm} = m_H = m_{h_S} = m_{A_S} = 800$ GeV and $\alpha_{h_S} = \alpha_{HS} = 0$.

We explore the interplay between $c_{\beta-\alpha}$ and singlet-double CP-odd Higgs A mixing α_{AS} in Fig. 10. The left panel presents the 95% C.L. allowed region in Δm_A vs. $c_{\beta-\alpha}$ for various $\alpha_{HS}=0$ (blue), $\pi/4$ (orange), and $\pi/2$ (green). The blue region in the left panel of Fig. 10 for $\alpha_{AS} = 0$ is consistent with the blue region in the right panel of Fig. 4. For larger α_{AS} , the allowed regions shift to the left, whereas the $c_{\beta-\alpha}$ bounds at both $m_A > m_{A_S}$ and $m_A < m_{A_S}$ become larger, due to the suppression of both the AHZ and AhZ terms by $c_{\alpha_{AS}}$. However, the $A_S hZ$ term is enhanced by $s_{\alpha_{AS}}$, which compensates the suppression of AHZ and AhZ . Therefore, the STU limit is relaxed faster at $m_A > m_{A_S}$ where A_S is less dominant in this

region. For $\alpha_{AS} = \pi/2$, only $A_S hZ$ contribution is left and contribution from A decouples. The 95% C.L. allowed region for $c_{\beta-\alpha}$ limit is a constant and independent of m_A . Since the role of A and A_S switches when $\alpha_{AS} \rightarrow \pi/2 - \alpha_{AS}$, the parameter space of $c_{\beta-\alpha}$ vs Δm_{A_S} is the same as the left panel of Fig. 10 with $\alpha_{AS} \rightarrow \pi/2 - \alpha_{AS}$.

The right panel of Fig. 10 presents the 95% C.L. allowed region in Δm_A vs. α_{AS} for various $|c_{\beta-\alpha}|=0$ (blue), 0.25 (orange) and 0.375 (green). The blue line indicates the same behavior of the STU dependence on (m_A, α_{AS}) as (m_H, α_{HS}) for $c_{\beta-\alpha} = 0$. However, these two cases differ when singlet admixture enters for $c_{\beta-\alpha} \neq 0$. The CP-odd Higgs A enters via AhZ and AHZ_s , where these contributions are suppressed when m_A is closed to m_H . In the case that $m_{A_S} = m_H$, the allowed regions only show up in the region of large α_{AS} are non-zero Δm_A , since A_S in this area is already dominated by the doublet properties. Similar to the left panel, the parameter space of α_{AS} vs Δm_{A_S} is the same as the right panel of Fig. 10 with $\alpha_{AS} \rightarrow \pi/2 - \alpha_{AS}$.

6 Interplay of electroweak and Higgs precision measurements

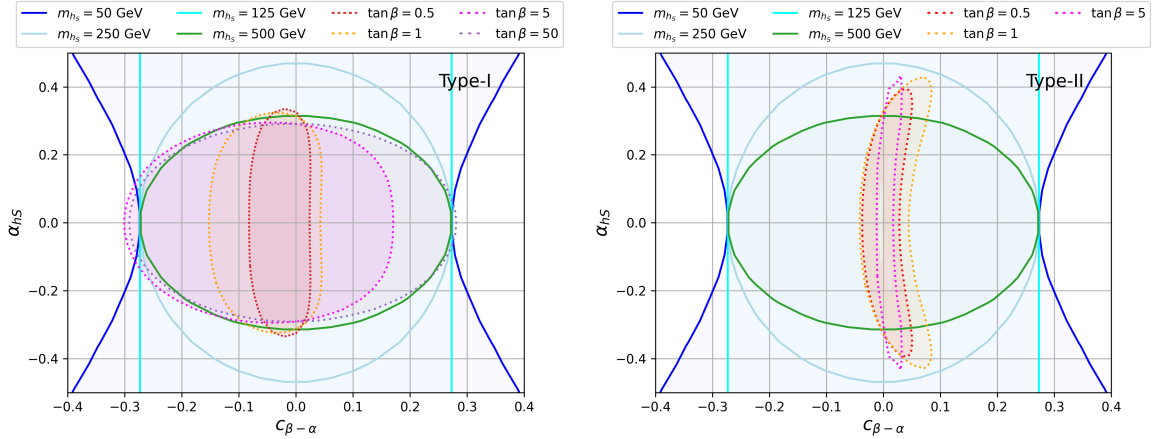


Figure 11. The parameter space of $c_{\beta-\alpha}$ vs α_{hS} , for $m_{h_S} = 50$ GeV (dark blue), 125 GeV (cyan), 250 GeV (light blue), 500 GeV (green), and $\tan \beta = 0.5$ (red), 1 (orange), 5 (magenta), and 50 (purple) under electroweak precision measurements (solid curves) and Higgs precision measurements (dashed curves). The other Higgs masses are $m_A = m_H = m_{H^\pm} = 800$ GeV, and $\alpha_{HS} = \alpha_{AS} = 0$. Left panel is for the type-I 2HDM+S and right panel is for the type-II 2HDM+S.

The precision measurements of the couplings of the 125 GeV Higgs at the LHC also place strong constraints on the parameter space of 2HDM+S, in particular, on $c_{\beta-\alpha}$, the singlet- h_{125} mixing α_{hS} , and $\tan \beta$. We perform the fit for 125 GeV Higgs properties with HiggsTools [22–26]. In Fig. 11, we present both 95% C.L. STU allowed region in $c_{\beta-\alpha}$ vs. α_{hS} place for various m_{h_S} (regions enclosed by solid curves) and 95% C.L. allowed region by 125 GeV Higgs precision measurements for various $\tan \beta$ (region enclosed by dashed curves) for the

Type-I (left panel) and the Type-II (right panel). Since the STU constraints only depend on the couplings of the Higgses with the gauge bosons, which is the same for different types of 2HDM, the solid curves are the same at both panels. For $m_{h_S} = 125$ GeV, the allowed range in $c_{\beta-\alpha}$ is independent of α_{h_S} . This is because $h_S VV$ and $h VV$ contribute the same for $m_h = m_{h_S}$, and α_{h_S} is not constrained as shown in the left plot of Fig. 5. For $m_{h_S} = 50$ GeV, a larger region of $c_{\beta-\alpha}$ can be accommodated for $\alpha_{h_S} \neq 0$ since the larger ΔT_1 can be compensated by $h_S VV$ with lighter m_{h_S} . While for $m_{h_S} > 125$ GeV, the allowed region in α_{h_S} shrinks, where the ΔT_1 and $h_S VV$ have the same sign in this mass region, which leads to tighter constraints.

For the Higgs precision on the Type-I 2HDM+S in the left panel, the allowed range of $c_{\beta-\alpha}$ gets weaker for larger $\tan \beta$. For $\tan \beta \gtrsim 5$, the electroweak precision measurements provide a stronger constraint on $c_{\beta-\alpha}$ at negative $c_{\beta-\alpha}$ region, while the Higgs precision measurements constrain the value of α_{h_S} better for $m_{h_S} \lesssim 500$ GeV. For $\tan \beta \sim 50$, the STU constraint on positive $c_{\beta-\alpha}$ can be stronger than Higgs precision measurement at $\alpha_{h_S} \sim 0$. Thus, the $|\alpha_{h_S}|$ in type-I model would be constrained to be less than 0.3 by the h_{125} coupling measurements, where the STU can provide a stronger α_{h_S} limit for $m_{h_S} > 500$ GeV.

For the Higgs precision on the Type-II 2HDM+S in the right panel, the allowed region in $c_{\beta-\alpha}$ is constrained to be much tighter, only a thin region around $c_{\beta-\alpha} \sim 0$. The constraints from the h_{125} coupling measurements are the weakest at $\tan \beta \sim 1$ and become stronger as $\tan \beta$ increases or decreases. $|\alpha_{h_S}|$ is constrained to be around 0.4, which is less dependent on the values of $\tan \beta$. The electroweak precision measurements provide a tight bound on the range of α_{h_S} for $m_{h_S} > 250$ GeV. A combination of the electroweak precision measurements and the Higgs precision measurements could help us to nail down the parameter space of 2HDM+S.

7 Conclusions

In this paper, we studied the implications of the oblique parameters, in particular, the T parameter, on the parameter space of the 2HDM+S model. Nine model parameters enter, including five masses m_H , m_{h_S} , m_A , m_{A_S} , m_{H^\pm} , and four mixing angles $c_{\beta-\alpha}$, α_{h_S} , α_{HS} and α_S . We identified five benchmark scenarios, Case-0 with $c_{\beta-\alpha} = 0$ and all the singlet mixing angles being 0 (the 2HDM alignment limit), and Case-I to IV with only one of the mixing angles being non-zero. We studied the 95% C.L. STU allowed region in the relevant parameter spaces. We found that

- **Case-0**

Other than the well known conclusion that the electroweak precision constraints are satisfied for $\Delta m_H = 0$ or $\Delta m_A = 0$, there is an upper limit on the mass splitting of $\Delta m_{H/A} \lesssim 900$ GeV for $m_{H^\pm} = 800$ GeV and $\Delta m_{A,H} = 0$, coming from the S parameter constraint. This upper limit also varies with m_{H^\pm} .

- **Case-I with $c_{\beta-\alpha} \neq 0$**
The constraint on $c_{\beta-\alpha}$ is weak for $m_H = 125$ GeV, $\Delta m_A = 0$, or $m_H = m_{H^\pm}$ and $\Delta m_A \sim -30$ GeV. The parameter space in $\Delta m_H - c_{\beta-\alpha}$ or $\Delta m_A - c_{\beta-\alpha}$ is significantly reduced for Δm_A or Δm_H away from 0.
- **Case-II with $\alpha_{h_S} \neq 0$**
 α_{h_S} is unconstrained for $m_{h_S} = 125$ GeV and $\Delta m_{H,A} = 0$. Allowed region shifts to larger m_{h_S} and $|\alpha_{h_S}|$ for $\Delta m_{A,H} \neq 0$.
- **Case-III with $\alpha_{HS} \neq 0$**
STU constraint can be satisfied for $c_{\alpha_{HS}}^2 m_H + s_{\alpha_{HS}}^2 m_{h_S} = m_{H^\pm}$ or $m_A = m_{H^\pm}$.
- **Case-IV with $\alpha_{AS} \neq 0$**
STU constraint can be satisfied for $c_{\alpha_{AS}}^2 m_A + s_{\alpha_{AS}}^2 m_{A_S} = m_{H^\pm}$ or $m_H = m_{H^\pm}$.

We further explored case-II - IV with non-zero $c_{\beta-\alpha}$, and observed that the singlet extension could compensate the $c_{\beta-\alpha}$ contribution and extend the allowed parameter space. Larger $|c_{\beta-\alpha}|$, however, typically leads to more constrained mass vs. mixing angle parameter space.

We also studied the complementarity between the electroweak precision analyses and Higgs coupling measurements. We found that for the Type-I scenario, electroweak precision measurements provide stronger constraints on α_S for $m_{h_S} > 500$ GeV, while Higgs coupling measurements constrain $c_{\beta-\alpha}$ better for $\tan \beta > 5$. For the Type-II scenario, the electroweak precision measurements provide a tight bound on the range of α_{h_S} for $m_{h_S} > 250$ GeV while the Higgs coupling measurements constrain $c_{\beta-\alpha}$ better for all values of $\tan \beta$.

In summary, the singlet extension of the 2HDM opens up the allowed parameter space when constraints from the electroweak precision measurements are considered. It also provides a complementary reach when combined with Higgs precision measurements. Our results are independent of the detailed symmetry assumption of Higgs sector and can be applied to the general case of the 2HDM+S. While our work studied benchmark scenarios with only one singlet mixing angle being nonzero, it identifies the main features of each mixing case, and provides a better understanding of a more comprehensive study in the most general mixing cases.

Acknowledgments

CL, JL and WS are supported by the Natural Science Foundation of China (NSFC) under grant numbers 12305115, Shenzhen Science and Technology Program (Grant No. 202206193000001, 20220816094256002), Guangdong Provincial Key Laboratory of Gamma-Gamma Collider and Its Comprehensive Applications(2024KSYS001), and Guangdong Provincial Key Laboratory of Advanced Particle Detection Technology(2024B1212010005). JL is also supported by the Fundamental Research Funds for the Central Universities, and the Sun Yat-sen University Science Foundation. SS is supported by the Department of Energy under Grant No. DEFG02-13ER41976/DE-SC0009913.

A Appendix

The STU observables are defined by

$$\alpha(m_Z)T = \frac{\Pi_{WW}(0)}{m_W^2} - \frac{\Pi_{ZZ}(0)}{m_Z^2}, \quad (\text{A.1})$$

$$\frac{\alpha(m_Z)}{4s_W^2 c_W^2} S = \frac{\Pi_{ZZ}(m_Z^2) - \Pi_{ZZ}(0)}{m_Z^2} - \frac{c_W^2 - s_W^2}{s_W c_W} \frac{\Pi_{Z\gamma}(m_Z^2)}{m_Z^2} - \frac{\Pi_{\gamma\gamma}(m_Z^2)}{m_Z^2}, \quad (\text{A.2})$$

$$\frac{\alpha(m_Z)}{4s_W^2} (S + U) = \frac{\Pi_{WW}(m_W^2) - \Pi_{WW}(0)}{m_W^2} - \frac{c_W}{s_W} \frac{\Pi_{Z\gamma}(m_Z^2)}{m_Z^2} - \frac{\Pi_{\gamma\gamma}(m_Z^2)}{m_Z^2}, \quad (\text{A.3})$$

where F , G and \hat{G} functions are defined as [17]

$$F(I, J) = \begin{cases} \frac{I+J}{2} - \frac{IJ}{I-J} \ln \frac{I}{J} & \text{for } I \neq J \\ 0 & \text{for } I = J \end{cases}, \quad (\text{A.4})$$

$$G(I, J, Q) = -\frac{16}{3} + \frac{5(I+J)}{Q} - \frac{2(I-J)^2}{Q^2} + \frac{r}{Q^3} f(I+J-Q, Q^2 - 2Q(I+J) + (I-J)^2) \\ + \frac{3}{Q} \left[\frac{I^2 + J^2}{I-J} - \frac{I^2 - J^2}{Q} + \frac{(I-J)^3}{3Q^2} \right] \ln \frac{I}{J}, \quad (\text{A.5})$$

$$\hat{G}(I, Q) = -\frac{79}{3} + 9\frac{I}{Q} - 2\frac{I^2}{Q^2} + \left(12 - 4\frac{I}{Q} + \frac{I^2}{Q^2} \right) \frac{f(I, I^2 - 4IQ)}{Q} \\ + \left(-10 + 18\frac{I}{Q} - 6\frac{I^2}{Q^2} + \frac{I^3}{Q^3} - 9\frac{I+Q}{I-Q} \right) \ln \frac{I}{Q}. \quad (\text{A.6})$$

with

$$f(r, t) = \begin{cases} \sqrt{r} \ln \left| \frac{t-\sqrt{r}}{t+\sqrt{r}} \right| & \text{for } r > 0 \\ 0 & \text{for } r = 0 \\ 2\sqrt{-r} \arctan \frac{\sqrt{-r}}{t} & \text{for } r < 0 \end{cases}. \quad (\text{A.7})$$

References

- [1] G. P. Salam, L.-T. Wang, and G. Zanderighi, *The Higgs boson turns ten*, *Nature* **607** (2022), no. 7917 41–47, [[arXiv:2207.00478](#)].
- [2] J. Gu, H. Li, Z. Liu, S. Su, and W. Su, *Learning from Higgs Physics at Future Higgs Factories*, *JHEP* **12** (2017) 153, [[arXiv:1709.06103](#)].
- [3] **ATLAS** Collaboration, G. Aad et al., *Observation of a new particle in the search for the Standard Model Higgs boson with the ATLAS detector at the LHC*, *Phys. Lett. B* **716** (2012) 1–29, [[arXiv:1207.7214](#)].
- [4] **CMS** Collaboration, S. Chatrchyan et al., *Observation of a New Boson at a Mass of 125 GeV with the CMS Experiment at the LHC*, *Phys. Lett. B* **716** (2012) 30–61, [[arXiv:1207.7235](#)].

- [5] A. Crivellin and B. Mellado, *Anomalies in particle physics and their implications for physics beyond the standard model*, *Nature Rev. Phys.* **6** (2024), no. 5 294–309, [[arXiv:2309.03870](#)].
- [6] H. Georgi, H. R. Quinn, and S. Weinberg, *Hierarchy of Interactions in Unified Gauge Theories*, *Phys. Rev. Lett.* **33** (1974) 451–454.
- [7] A. G. Cohen, D. B. Kaplan, and A. E. Nelson, *Progress in electroweak baryogenesis*, *Ann. Rev. Nucl. Part. Sci.* **43** (1993) 27–70, [[hep-ph/9302210](#)].
- [8] G. Bertone, D. Hooper, and J. Silk, *Particle dark matter: Evidence, candidates and constraints*, *Phys. Rept.* **405** (2005) 279–390, [[hep-ph/0404175](#)].
- [9] S. P. Martin, *A Supersymmetry primer*, *Adv. Ser. Direct. High Energy Phys.* **18** (1998) 1–98, [[hep-ph/9709356](#)].
- [10] G. C. Branco, P. M. Ferreira, L. Lavoura, M. N. Rebelo, M. Sher, and J. P. Silva, *Theory and phenomenology of two-Higgs-doublet models*, *Phys. Rept.* **516** (2012) 1–102, [[arXiv:1106.0034](#)].
- [11] M. Muhlleitner, M. O. P. Sampaio, R. Santos, and J. Wittbrodt, *The N2HDM under Theoretical and Experimental Scrutiny*, *JHEP* **03** (2017) 094, [[arXiv:1612.01309](#)].
- [12] S. Baum and N. R. Shah, *Two Higgs Doublets and a Complex Singlet: Disentangling the Decay Topologies and Associated Phenomenology*, *JHEP* **12** (2018) 044, [[arXiv:1808.02667](#)].
- [13] U. Ellwanger, C. Hugonie, and A. M. Teixeira, *The Next-to-Minimal Supersymmetric Standard Model*, *Phys. Rept.* **496** (2010) 1–77, [[arXiv:0910.1785](#)].
- [14] J. Dutta, J. Lahiri, C. Li, G. Moortgat-Pick, S. F. Tabira, and J. A. Ziegler, *Dark Matter Phenomenology in 2HDMS in light of the 95 GeV excess*, [arXiv:2308.05653](#).
- [15] S. Heinemeyer, C. Li, F. Lika, G. Moortgat-Pick, and S. Paasch, *Phenomenology of a 96 GeV Higgs boson in the 2HDM with an additional singlet*, *Phys. Rev. D* **106** (2022), no. 7 075003, [[arXiv:2112.11958](#)].
- [16] M. E. Peskin and T. Takeuchi, *Estimation of oblique electroweak corrections*, *Phys. Rev. D* **46** (1992) 381–409.
- [17] W. Grimus, L. Lavoura, O. M. Ogreid, and P. Osland, *The Oblique parameters in multi-Higgs-doublet models*, *Nucl. Phys. B* **801** (2008) 81–96, [[arXiv:0802.4353](#)].
- [18] J. Haller, A. Hoecker, R. Kogler, K. Mönig, T. Peiffer, and J. Stelzer, *Update of the global electroweak fit and constraints on two-Higgs-doublet models*, *Eur. Phys. J. C* **78** (2018), no. 8 675, [[arXiv:1803.01853](#)].
- [19] J. Erler and A. Freitas, *Electroweak model and constraints on new physics*, [pdg.lbl.gov/2024/reviews/rpp2024-rev-standard-model](#) (2024).
- [20] **Gfitter** Collaboration, M. Baak, M. Goebel, J. Haller, A. Hoecker, D. Kennedy, K. Moenig, M. Schott, and J. Stelzer, *Updated Status of the Global Electroweak Fit and Constraints on New Physics*, *Eur. Phys. J. C* **72** (2012) 2003, [[arXiv:1107.0975](#)].
- [21] M. Gorbahn, J. M. No, and V. Sanz, *Benchmarks for Higgs Effective Theory: Extended Higgs Sectors*, *JHEP* **10** (2015) 036, [[arXiv:1502.07352](#)].
- [22] H. Bahl, T. Biekötter, S. Heinemeyer, C. Li, S. Paasch, G. Weiglein, and J. Wittbrodt, *HiggsTools: BSM scalar phenomenology with new versions of HiggsBounds and HiggsSignals*, *Comput. Phys. Commun.* **291** (2023) 108803, [[arXiv:2210.09332](#)].

- [23] P. Bechtle, S. Heinemeyer, O. Stål, T. Stefaniak, and G. Weiglein, *HiggsSignals: Confronting arbitrary Higgs sectors with measurements at the Tevatron and the LHC*, *Eur. Phys. J. C* **74** (2014), no. 2 2711, [[arXiv:1305.1933](#)].
- [24] O. Stål and T. Stefaniak, *Constraining extended Higgs sectors with HiggsSignals*, *PoS EPS-HEP2013* (2013) 314, [[arXiv:1310.4039](#)].
- [25] P. Bechtle, S. Heinemeyer, O. Stål, T. Stefaniak, and G. Weiglein, *Probing the Standard Model with Higgs signal rates from the Tevatron, the LHC and a future ILC*, *JHEP* **11** (2014) 039, [[arXiv:1403.1582](#)].
- [26] P. Bechtle, S. Heinemeyer, T. Klingl, T. Stefaniak, G. Weiglein, and J. Wittbrodt, *HiggsSignals-2: Probing new physics with precision Higgs measurements in the LHC 13 TeV era*, *Eur. Phys. J. C* **81** (2021), no. 2 145, [[arXiv:2012.09197](#)].